Femtosecond phononic coupling to both spins and charges in a room-temperature antiferromagnetic semiconductor

D. Bossini ◉,[1,2,*] S. Dal Conte,[3,4] M. Terschanski,[2] G. Springholz,[5] A. Bonanni,[5] K. Deltenre,[2]
F. Anders,[2] G. S. Uhrig ◉,[2] G. Cerullo,[3,4] and M. Cinchetti ◉[2]

[1]*Department of Physics and Center for Applied Photonics, University of Konstanz, D-78457 Konstanz, Germany*
[2]*Department of Physics, TU Dortmund University, Otto-Hahn Straße 4, 44227 Dortmund, Germany*
[3]*Dipartimento di Fisica, Politecnico di Milano, Piazza Leonardo da Vinci 32, Milano, Italy*
[4]*Istituto di Fotonica e Nanotecnologie, Consiglio Nazionale delle Ricerche, Piazza Leonardo da Vinci 32, Milano, Italy*
[5]*Institute of Semiconductor and Solid State Physics, Johannes Kepler University Linz, Altenbergerstr. 69, 4040 Linz, Austria*

Spintronics is postulated on the possibility to employ the magnetic degree of freedom of electrons for computation and couple it to charges. In this view the combination of the high frequency of spin manipulations offered by antiferromagnets, with the wide tunability of the electronic properties peculiar of semiconductors, provides a promising and intriguing platform. Here we explore this scenario in α-MnTe, which is a semiconductor antiferromagnetically ordered at room temperature. Relying on a Raman mechanism and femtosecond laser pulses, we drive degenerate modes of coherent optical phonons, which modulate the chemical bonds involved in the superexchange interaction. The spectrally resolved measurements of the transient reflectivity reveal a coherent modulation of the band gap at the frequency of 5.3 THz. The detection of the rotation of the polarization, typically associated with magneto-optical effects, shows coherent and incoherent contributions. Modeling how the ionic motion induced by the phonons affects the exchange interaction in the material, we calculate the photoinduced THz spin dynamics: the results predict both a coherent and incoherent response, the latter of which is consistent with the experimental observation. Our work demonstrates that the same phonon modes modulate both the charge and magnetic degree of freedom, suggesting the resonant pumping of phonons as a viable way to link spin and charge dynamics even in nonlinear regimes.

I. INTRODUCTION

One of the overarching goals of solid state physics in the last 30 years has been to establish magnetic semiconductors as a platform for dissipationless spintronics [1–3]. The main hindrance to this breakthrough is the difficulty to synthesize a room-temperature ferromagnetic semiconductor. Recently, the spintronic capabilities of metallic and dielectric antiferromagnets (AFs) have been deeply investigated [4–6], confirming the feasibility of spin manipulation even at extreme timescales [7,8]. Here we measure the time-dependent optical properties of the room-temperature antiferromagnetic semiconductor MnTe. Ultrafast spintronics in semiconductors requires the ability to couple the magnetic and electronic degrees of freedoms, the latter being strongly defined by the band gap, in the femtosecond regime. We demonstrate that the displacive excitation [9,10] of an optical phonon modulates coherently the band gap at a 5.3 THz frequency. Our data show that the same lattice mode couples also to spins. We derive a model revealing the nature of this phenomenon and predicting the spin dynamics induced by this coupling, whose signatures are observed in the time-resolved magneto-optical response. Given the simultaneous dynamical coupling to both spins and charges, the selective resonant excitation of optical phonons emerges as a tool to advance towards the long sought-after realization of efficient and controllable semiconductor spintronics.

This paper is organized as follows. We introduce in Sec. II the material here investigated and the experimental methods, discussing both the setup and the magneto-optical effects allowed in our detection geometry. In Sec. III we present the time- and spectrally resolved measurements of the reflectivity of α-MnTe. The optical dynamics detected via single-color experiments, revealing the generation of coherent phonons, is shown and discussed in Sec. IV. In Sec. V our model of the spin dynamics induced by the optically generated phonons is reported. The measurement of the magneto-optical dynamics is the subject of Sec. VI. We summarize the conclusions and formulate the perspectives of our work in Sec. VII.

II. METHODS AND MATERIALS

A. Material

We investigate hexagonal manganese telluride (α-MnTe). This material is a correlated magnetic semiconductor comprising two antiferromagnetically coupled magnetic sublattices [Mn$^{\Uparrow,\Downarrow}$ in Fig. 1(a)], which originate a long-range order above room temperature (Néel temperature $T_N \approx 307$ K
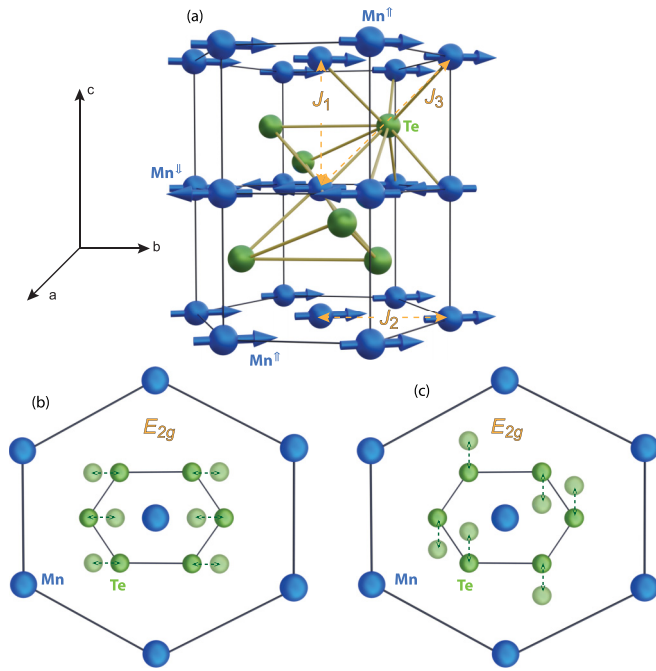
———————
*davide.bossini@uni-konstanz.de

FIG. 1. Structure and lattice modes of α-MnTe. (a) Crystallographic and magnetic structure of α-MnTe. The three superexchange couplings are shown by the yellow dashed arrows [11]: J_1 is the dominating antiferromagnetic superexchange interaction, J_2 is a weaker ferromagnetic coupling between Mn atoms within the ferromagnetic hexagonal planes, the Te-mediated J_3 is the weakest interaction and it is antiferromagnetic, involving 12 next-nearest neighbor sites. (b) and (c) Displacement of Te atoms induced by the degenerate E_{2g} modes. The identification of the atomic displacement is done by comparing α-MnTe to the isomorphic MgB_2 [12].

FIG. 2. MLD in α-MnTe. (a) Orientation of the Néel vector for one of the three possible antiferromagnetic domains [13]. The electric field of the probe beam has components along both the direction of spins and the direction perpendicular to them. (b) Rotation of the polarization induced by magnetic linear dichroism for a probe beam propagating through the sample.

[11,13,14]). The reported band-gap $E_{\mathrm{gap}} \approx (1.27–1.46)$ eV is indirect [13]. α-MnTe crystallizes in the NiAs structure[15] shown in Fig. 1(a) and has a centrosymmetric point group (6/*mmm*), in which the collective ionic vibrations of the Te atoms displayed in Figs. 1(b) and 1(c) represent Raman-active optical phonons. As such, the nearest neighbors Te atoms oscillate out-of-phase as shown in Figs. 1(b) and 1(c). Considering that Mn and Te ions are charged, the ionic oscillations represented in Figs. 1(b) and 1(c) induce transient dipole moments and, thus, local electric fields during the lattice motion. Our specimen of α-MnTe is grown by molecular beam epitaxy on a SrF_2(111) substrate using elemental Mn and Te sources and substrates temperatures in the range (370–450) °C. Two-dimensional growth is achieved in both cases as inferred from the streaked reflection high energy electron diffraction (RHEED) patterns observed during the growth. The epitaxial relation between the MnTe overlayer and the substrate is $(0001)[10\bar{1}0]_{\mathrm{MnTe}}||(111)[11\bar{2}]_{\mathrm{sub}}$.

B. Pump-probe setup

For the pump-probe experiments a regeneratively amplified mode-locked Ti:sapphire laser, providing 100 fs, 500 μJ pulses at 800 nm and 2 kHz repetition rate is used. For broadband transient reflectivity measurements (Fig. 3) the α-MnTe sample is photoexcited by a broadband pulse cen-
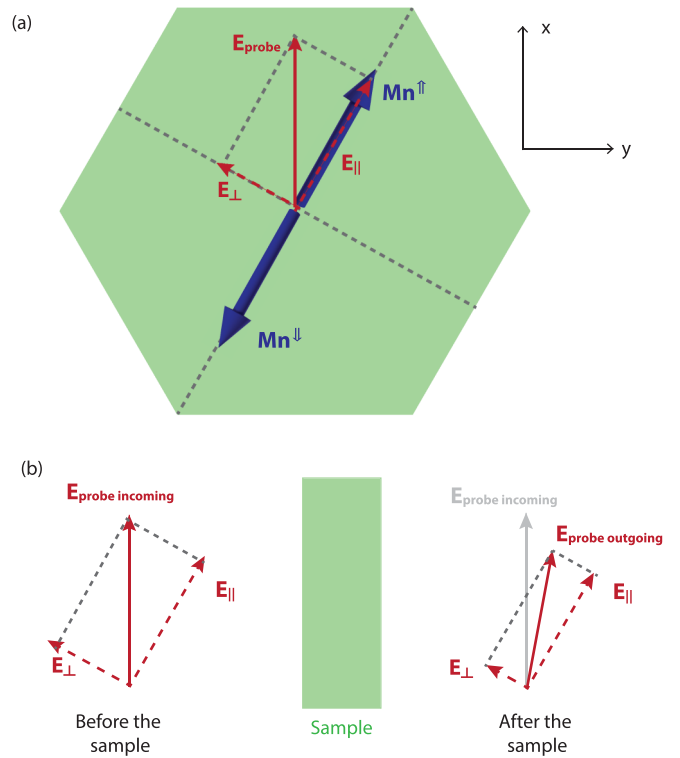
tered at 2.4 eV generated by a home-built noncollinear optical parametric amplifier (NOPA). The pulse is temporally compressed to nearly 15 fs by a pair of custom-made chirped mirrors. The transient optical response of the sample is measured by a white-light probe generated in a 2-mm-thick sapphire plate. After the generation, the fundamental wavelength beam is removed by a short-pass filter. The rms fluctuation of white light is around 0.2%. The pump and probe spot sizes at the sample position are 100 and 70 μm, respectively. The reflected probe is dispersed by a grating and detected by a Si CCD camera with 532 pixels. The pump pulse is modulated at 1 kHz by a mechanical chopper, resulting in a detection sensitivity of the order of 10^{-4} with an integration time of 2 s.

For the transient transmissivity and polarization rotation measurements (Fig. 8) the probe is generated by a second NOPA, filtered around 1.72 eV, and collected by a balanced photodetector, consisting of two photodiodes followed by a differential amplifier. The Wollaston prism separates the two orthogonally polarized components of the probe beam [Fig. 6(a)]. We rotate the Wollaston prism in order to equalize the probe intensities on the two photodiodes. The pump-induced imbalance of the signal is measured by a lock-in amplifier which is locked to the modulation frequency of the pump beam (i.e., 1 kHz). The sample has been placed in a cryostat, allowing to cool it down to liquid nitrogen temperature.
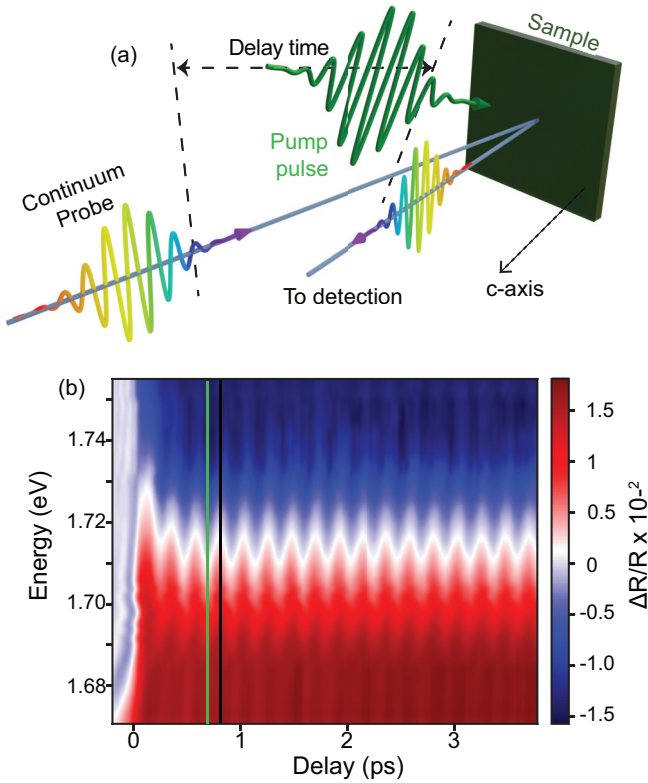
FIG. 3. Time- and spectrally resolved femtosecond dynamics of the band gap of MnTe. (a) The pump beam with a central photon energy of 2.4 eV impinges on the sample, triggering dynamics of the reflectivity. The transient reflectivity in the 1.65–2.76 eV spectral range is monitored by white light continuum pulses, which are delayed in a controlled and continuously variable way from the excitation pulses. (b) Spectrally and time-resolved dynamics of the reflectivity of α-MnTe triggered by a linearly polarized pump beam. The fluence is set to 60 μJ/cm^2 and the temperature of the sample is 77 K. Oscillations at the frequency of 5.3 THz are visible in the spectral band centered at 1.71 eV, 50 meV wide. The two vertical lines show two selected pump-probe delays corresponding to a maximum and minimum of the oscillations of E_{gap}.

C. Magneto-optical detection

Time-resolved spin dynamics in antiferromagnets can be typically detected by means of quadratic magneto-optical effects affecting the probe beam. The dielectric tensor describing the interaction between α-MnTe and the probe beam, propagating along the z axis (reference frame in Fig. 2) is given by

$$\epsilon = \begin{pmatrix} \epsilon_{xx} & \epsilon_{xy} & 0 \\ \epsilon_{yx} & \epsilon_{yy} & 0 \\ 0 & 0 & 0 \end{pmatrix}. \tag{1}$$

In an antiferromagnetic material the symmetric components can be expanded [16] as

$$\epsilon_{ii} = \epsilon_{ii}^0 + \chi_{kl}L_kL_l + \xi_{klmn}L_kL_lL_mL_n + \cdots, \tag{2}$$

where L_i are the components of the Néel vector. The first term is spin independent and describes the refraction (real part)

and the optical absorption (imaginary part) of the material. The following terms contain even powers of spin multiplied by material-dependent tensors. The second term describes quadratic-magneto-optical effects, which are common in antiferromagnets [8,17]. We report here a symmetry analysis of α-MnTe in the experimental geometry shown in Fig. 2. The hexagonal α-MnTe belongs to the 6/mmm point group, therefore the light-matter interaction originating quadratic magneto-optical effects in general is described by the following contribution to the thermodynamic potential:

$$\Phi = \chi_{ijkl}E_iE_jL_kL_l, \tag{3}$$

where i, j, k, l are cartesian coordinates. In Eq. (3) χ_{ijkl} is a fourth-rank polar tensor, $E_{i,j}$ are the components of the electric field of the pump beam, and $L_{k,l}$ are components of the Néel vector. In the reference frame shown in Fig. 2, the electric field of the probe beam was linearly polarized along the the x axis and propagating along the z axis. The Néel vector has components along both the x and y axis (Fig. 2), given the domain structure of an hexagonal antiferromagnet [13]. Considering the specific case of magnetic linear dichroism, the antiferromagnetic vector has to be considered quadratically [18], so we obtain

$$\begin{aligned} \Phi &= \chi_{iijj}E_iE_iL_jL_j \\ &= \chi_{xxxx}E_xE_xL_xL_x + \chi_{xxyy}E_xE_xL_yL_y. \end{aligned} \tag{4}$$

The components of χ satisfy the symmetries of the 6/mmm point group [19], namely $\chi_{xxyy} = 1/3 \cdot \chi_{xxxx} \neq 0$ showing that magnetic linear dichroism is allowed by symmetry in α-MnTe.

Figure 2(a) schematically represents the magnetic linear dichroism in α-MnTe in our experimental geometry. A Mn atom is located in correspondence of each corner of the hexagon. Considering one of the three in-plane easy axes of this material as the direction along which spins are aligned, we can identify a parallel and a perpendicular direction to the antiferromagnetic vector. The probe beam has electric field parallel to the x axis, which means that it has both a nonzero parallel and a nonzero perpendicular component with respect to the direction of the Néel vector. As a consequence, it experiences the absorption coefficients along these two directions, which differs because of the magnetic contributions to the dielectric tensor. In the case of a dissipative light-matter interaction regime, these terms and Imϵ_{ii}^0 can affect the rotation of the polarization via linear dichroism, which is magnetic if spin-dependent terms are involved: magnetic linear dichroism (MLD) induces thus a rotation of the polarization quadratically proportional to spins. Therefore, the ratio $E_\parallel/E_\perp$ for the probe beam transmitted through the sample is different from the value of this ratio for the probe beam impinging on the sample. This change in the $E_\parallel/E_\perp$ ratio induces a rotation of the electric field of the probe beam and, thus, of the polarization [Fig. 2(b)]. We note that in the reference frame displayed in Fig. 2(a), a linear combination of L_x and L_y expresses the purely longitudinal spin dynamics. As reported in the literature [8,17,20,21], this magneto-optical effect can be employed in pump-probe experiments to detect the transient longitudinal demagnetization of the sublattices in an AF.
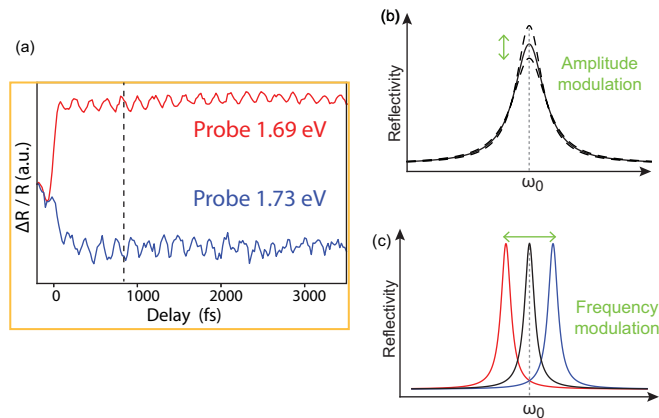
FIG. 4. Coherent modulation of the band gap. (a) The oscillations of $\Delta R/R$ for the selected spectral components of the supercontinuum probe are out-of-phase by π. (b) Amplitude modulation of a Lorentz oscillator: The spectral components at both sides of the resonance frequency (ω_0) oscillate in-phase. (c) Frequency modulation of a Lorentz oscillator: The spectral components at the blue and red sides of the resonance frequency (ω_0) oscillate out-of-phase by π. This modulation is consistent with the data shown in Fig. 3(b).

We now move on discussing the measurements of the transient reflectivity performed with both temporal and spectral resolution.

III. TIME- AND SPECTRALLY RESOLVED OPTICAL MEASUREMENTS

We perform a femtosecond pump-probe experiment, in which the transient reflectivity ($\Delta R/R$) of α-MnTe is detected in the (1.65–2.76) eV spectral range [Fig. 3(a)]. The combination of high temporal and spectral resolution of this approach allows us to fully track the photodriven transient evolution of E_{gap}. The color map in Fig. 3(b) shows two spectral regions with a different sign of the signal: negative above 1.71 eV and positive below. Interestingly, in a spectral range centered at 1.71 eV, which corresponds to the rising edge of the band gap [22,23], pronounced oscillations at the frequency of 5.3 THz are visible. This value is consistent with the frequency of two degenerate E_{2g} phonon modes observed in the Raman spectrum of α-MnTe [24]. These lattice modes imply oscillations of Te atoms, as displayed in Figs. 1(b) and 1(c).

Selecting one probe photon energy just above and just below the central value of 1.71 eV [Fig. 4(a)], we observe that the oscillations of the reflectivity are out-of-phase by π. To understand the phase of the oscillations we model the band gap of α-MnTe by a simple Lorentz oscillator, modulated by the optically activated phonon. A modulation of the amplitude [Fig. 4(b)] triggers oscillations of all the spectral components in phase with each other. In contrast, if the frequency [ω_0 in Figs. 4(b) and 4(c)] is modulated [Fig. 4(c)], the spectral components on the higher-energy side of ω_0 oscillate with a phase difference of π with respect to the components on the lower-energy side of the central frequency. This latter scenario is consistent with our data and points to the conclusion that the band gap is coherently modulated at the frequency of 5.3 THz.

TABLE I. Comparison efficiency. The data for Si and GaAs are taken from the literature [25].

Material	Fluence	$\Delta R/R$
Si	300 μJ /cm^2	10^{-5}
GaAs	170 μJ /cm^2	10^{-4}
α-MnTe	60 μJ /cm^2	10^{-2}

The degenerate E_{2g} lattice modes are optical, so as already mentioned in Sec. II, they induce a transient local electric field, which can shift the spectral lines via a Stark-like effect. This phenomenon has been experimentally already observed in both direct (GaAs) and indirect (Si) band-gap semiconductors [25].

A quantitative comparison of the efficiency of the process is reported in Table I. The data in Fig. 3(b) are obtained by pumping α-MnTe with mere 60 μJ/cm^2 and the $\Delta R/R$ modulation observed (1.5×10^{-2}) is two orders of magnitude higher than in GaAs, despite the fluence being three times smaller. We thus conclude that the lattice-E_{gap} coupling in α-MnTe induces a much stronger transient modulation of the reflectivity in comparison with the samples investigated in the literature [25]. Ascertaining whether this difference is due to the cross section of the displacive excitation mechanism or to the coupling between the lattice mode and the profile of the band structure is beyond the scope of the current paper. Moreover, we are interested in estimating the value of the band-gap modulation observed in Fig. 3(b). The intrinsic temporal chirp of the supercontinuum due to the group velocity dispersion must be taken into account [26]. This effect is visible at the femtosecond timescale. The chirp is numerically corrected by separately analyzing the transient reflectivity for each wavelength of the supercontinuum probe beam. In particular, the first derivative of each pump-probe scan is calculated. Then the maximum of the first derivative is defined as zero delay time.

In Fig. 3(b) the white stripe representing the phonon oscillation corresponds to a vanishing value of the transient reflectivity. Hence we consider two pump-probe delays, at which a maximum and a minimum of the phonon are observed [vertical lines in Fig. 3(b)]. The procedure employed to estimate the amplitude of the band-gap modulation is shown in Fig. 5. The reflectivity spectra corresponding to the black and green lines displayed in Fig. 3(b) are plotted, highlighting the energy region corresponding to a zero value of the reflectivity (blue circle). The difference in the values of the energy at which the reflectivity vanishes is taken as a direct estimation of the amplitude of the band-gap modulation. The results is $\Delta E_{\text{gap}} \approx 5.5$ meV $\approx 4 \times 10^{-3}$ of the original value.

The value of the energy gap and the sublattice magnetizations in α-MnTe are coupled in equilibrium, as E_{gap} is blueshifted in the AF phase by an amount proportional to the modulus of the sublattice magnetization [Mn$^{\Uparrow,\Downarrow}$ in Fig. 1(a)] [22,23]. The existence of an out-of-equilibrium coupling between these quantities on the femtosecond timescale can be experimentally assessed by comparing the optical and magneto-optical dynamics in the paramagnetic (at $T =$
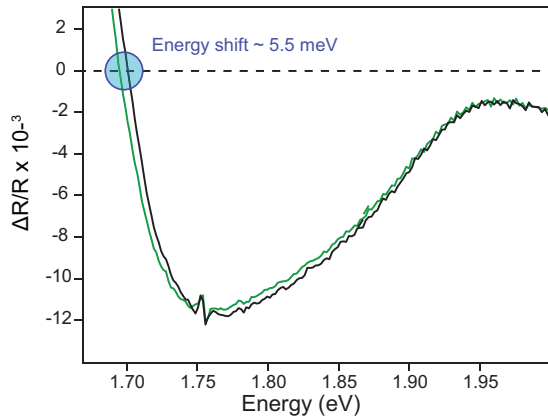
FIG. 5. Extrapolation ΔE_{gap}. Transient reflectivity for the selected pump-probe delays. The value of the energy at which the zero value [i.e., max or minimum of the oscillation in Fig. 3(b)] is crossed is considered for both traces. The difference of these two energy values is an estimation of the amplitude of the band-gap modulation.

320 K) and antiferromagnetic (at $T = 77$ K) phases. Such comparison requires single-color measurements.

IV. SINGLE-COLOR OPTICAL PUMP-PROBE MEASUREMENTS

We directly detect the photoinduced optical response of α-MnTe by tracking the time-resolved transmissivity with a narrow-band, i.e., *single-color*, optical probe beam. The photon energy of the probe beam was set to 1.72 eV, since at this photon energy a strong signal was observed in Fig. 3(b). The setup employed, described in Sec. II and shown in Fig. 6(a), allows the simultaneous detection of the transient transmissivity ($\Delta T/T$) and the rotation of the polarization. In this section we discuss the $\Delta T/T$ dynamics.

The data taken in the first 3.5 ps after the photoexcitation [Fig. 6(b)] show that the 5.3 THz phonon is induced and detected in both the paramagnetic and the antiferromagnetic phases. In particular, the initial phase of the oscillation is cosinelike in both traces, strongly suggesting that the lattice modes are triggered via a displacive mechanism [9,10]. The essence of this mechanism is that the excitation of electrons from an occupied to an unoccupied state alters the interionic potentials so that the previous atomic positions are no longer equilibrium positions. The ions thus begin moving towards the minima of the modified potential, at the frequency determined by the dispersion relation of phonons. The excitation photon energy employed in our experiments is above E_{gap}, so the pump beam actively promotes electrons in the initially unoccupied conduction band triggering the displacive phonon excitations.

Figure 6(b) shows that the oscillations in the two data sets are not in phase anymore at a delay of ≈ 3 ps, hinting towards a temperature dependence of the phonon frequency. Hence we consider the Fourier transform of the data in Fig. 6(c): both the frequency and the linewidth of the lattice mode are affected by temperature. More precisely, the frequency is lower, and the damping time is shorter in the paramagnetic phase, pointing at an intimate connection between the
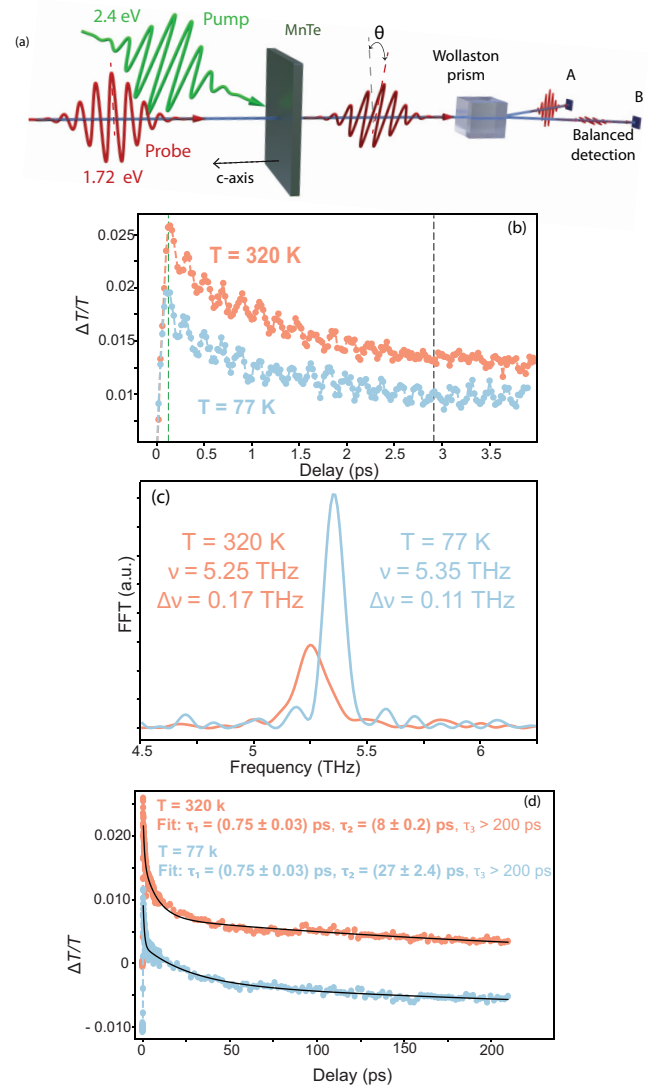

FIG. 6. Temperature-dependent optical dynamics. (a) Setup to measure the transient transmissivity and rotation of the polarization. The sum of the signals from the two diodes (A + B) is a measurement of $\Delta T/T$, while θ is given by the difference (A − B) in the balanced detection scheme. The selected probe photon energy corresponds to the maximum signal in Fig. 3(b), while the pump photon energy is the same as in the experiment reported in Fig. 3. (b) Transient transmissivity measured in the paramagnetic ($T = 320$ K) and antiferromagnetic ($T = 77$ K) phases. (c) Fourier transform of the data in (b). (d) Transient transmissivity in the paramagnetic and antiferromagnetic phase detected in a 200 ps delay range.

antiferromagnetic order and the E_{2g} phonons. In solids the frequency and lifetime of lattice vibrations may be temperature dependent, regardless of any coupling to spins. This is indeed the case also for several phonon modes in α-MnTe, as reported by temperature-dependent Raman scattering data [24]. However, the same experiment reveals that the temperature dependence of the 5.3 THz lattice mode differs from the one of the other phonons, as the long-range antiferromagnetic order is established (i.e., below T_N [24]). More in details, the frequency of the 5.3 THz mode increases as the temperature is lowered in a more pronounced way than in

the case of the other phonons. The temperature dependence of the linewidth displays a discontinuity in correspondence of the magnetic phase transition. Both features are unique of this specific mode [24]. The measurements reported here confirm the spin-phonon coupling in the frequency domain from the spectral analysis in Fig. 6(c). Furthermore, the time evolution of the phase of the oscillations in the two time traces in Fig. 6(b) expresses the consequences of the spin-lattice coupling in the time domain. In fact, the two curves exhibit oscillations which are out-of-phase at a delay time of 3 ps, as the eigenfrequency of the phonon is temperature dependent because of the spin-phonon coupling.

Figure 6(d) shows $\Delta T/T$ dynamics measured over an extended timescale, fitted with a function containing three exponentially decaying terms. The first relaxation has a characteristic time $\tau_1 = (750 \pm 30)$ fs and is temperature independent. Since the pump beam with 2.4 eV photon energy promotes electrons to the conduction band with excess energy, we associate τ_1 with the relaxation of such carriers via electron-phonon scattering. In contrast, the characteristic time τ_2 is affected by temperature. Interestingly, the variation of τ_2, from 8 to 27 ps, matches quantitatively the variation of the recently calculated lattice thermal conductivity [14] from 2 W/(m K) at 300 K to 7.5 W/(m K) at 100 K. A first-principle treatment of this problem shows that the phonon thermal conductivity depends on the characteristic phonon-phonon and electron-phonon scattering times [27]. Therefore, we associate the time constant τ_2 [see fit in Fig. 6(d)] with the phonon-phonon scattering time. The data show also a third exponential relaxation τ_3, likely due to heat diffusion from the excited volume. The time constant τ_3 exceeds the observation window and therefore it is not further discussed.

The data discussed so far reports unambiguously the optical activation of coherent phonons. These modes are coupled to the magnetic system and, in the next section, we derive a model predicting which spin dynamics is triggered by the collective lattice oscillations.

V. THEORY

In Sec. II we have already mentioned that the E_{2g} phonons induce an ionic displacement which modulates the angle between the bonds involved in the Mn-Te-Mn superexchange pattern [Figs. 1(b) and 1(c)]. A phonon able to induce such an atomic motion has been experimentally demonstrated to couple to the macroscopic magnetic order in Heisenberg antiferromagnets [28]. However, *a priori* it is not trivial to predict how the generation of the 5.3 THz lattice mode affects the spin dynamics. Moreover, the nature of the microscopic coupling between the lattice mode and the spins in α-MnTe is an open issue. In the following we derive a model in which the phonon directly modulates the exchange interaction, and discuss the consequences of such perturbation for the dynamics of the antiferromagnetic order parameter. We emphasize that our model does not rely on quasistatic shifts of the coupling constants due to anharmonicities, as done in other studies [29,30]. Microscopically the process we are considering is analog to a parametric conversion: the phonon drives pairs of magnon modes with equal and opposite wave vector, originating from spin-flip events in different sublattices, thus fulfilling

both spin ($\Delta S = 0$) and wave-vector conservation ($\Delta \boldsymbol{k} = 0$). Consequently, pairs of counterpropagating magnons with half the frequency of the phonon are created. From the dispersion relation of spin waves in α-MnTe [14], we conclude that these magnons have a wave vector neither at the center nor at the edges of the Brillouin zone, but in between. Importantly, no torque on the spins is applied (since $\Delta S = 0$), hence the direction of the sublattice magnetization is unchanged. We model the spin dynamics of α-MnTe considering the equilibrium Hamiltonian

$$H = \sum_{\langle i,j \rangle_z} J_1 \vec{S}_i \vec{S}_j + \sum_{\langle i,j \rangle_{xy}} J_2 \vec{S}_i \vec{S}_j + \sum_{\langle\langle i,j \rangle\rangle} J_3 \vec{S}_i \vec{S}_j, \tag{5}$$

where J_i denote the Heisenberg couplings between the spins $\vec{S}_i$ and $\vec{S}_j$ with the couplings J_1 between interlayer nearest neighbors, J_2 between nearest neighbors in a Mn plane, and J_3 between third-nearest neighbors. The effect of the pump pulses on the system is expressed via the excitation of the E_{2g} phonons which, as aforementioned, modulate the exchange interaction. We thus express such perturbation as

$$\frac{\delta J_3(t)}{J_1 S} \equiv a(t) = a_0 \exp(-\gamma t) \cos(\omega_0 t), \tag{6}$$

where a_0 parametrizes the maximum value of the change of J_3, ω_0 denotes the phonon frequency, and γ specifies the damping of the phonon mode. By adding this term to the Hamiltonian in Eq. (5) and relying on the Heisenberg equation of motion for operators ($\frac{d\hat{A}}{dt} = i\langle[H(t), \hat{A}]\rangle$, where $\hat{A}$ is a generic operator), we can calculate the time-dependent order parameter $\vec{L} \equiv \text{Mn}^{\Uparrow} - \text{Mn}^{\Downarrow}$. Details of the calculations can be found elsewhere [31]. For the Heisenberg couplings in equilibrium, we use the parameter set of Ref. [11]. Note that we have to include a factor of 2 and that we use another sign convention due to a slightly different definition of the Hamiltonian compared to Ref. [11]. We represent the spins by bosonic operators via the Holstein-Primakoff representation [32] and keep only bilinear terms in the Hamiltonian (linear spin wave theory). We apply a Fourier and a Bogoliubov transformation to diagonalize the equilibrium problem in $\vec{k}$ space and obtain

$$\frac{\tilde{H}_0}{J_1 S} = \sum_{\vec{k}} \omega_{\vec{k}} b_{\vec{k}}^\dagger b_{\vec{k}} + E_d + \Delta E, \tag{7a}$$

with $\omega_{\vec{k}} = \sqrt{A_{\vec{k}}^2 - B_{\vec{k}}^2}$, $\tag{7b}$

$$A_{\vec{k}} = \frac{1}{J_1}[2J_1 - 6J_2 + 12J_3 + J_2\gamma_\Delta(\vec{k})], \tag{7c}$$

$$B_{\vec{k}} = 2\cos(k_z)\left[1 + 2\frac{J_3}{J_1}\gamma_\Delta(\vec{k})\right], \tag{7d}$$

$$\gamma_\Delta(\vec{k}) = \cos(k_x) + \cos\left(\frac{\sqrt{3}}{2}k_y + \frac{1}{2}k_x\right)$$
$$+ \cos\left(-\frac{\sqrt{3}}{2}k_y + \frac{1}{2}k_x\right), \tag{7e}$$

where $\omega_{\vec{k}}$ denotes the magnon frequency and $b_{\vec{k}}^\dagger b_{\vec{k}}$ stands for the magnon occupation operator. The contributions to the ground state energy E_d and ΔE arise from the Fourier and Bogoliubov transformation, respectively. Since they do not enter

into the equations of motion that we calculate in the next step, further treatment is not necessary at this point. Considering that the Heisenberg couplings J_i oscillate, the Hamiltonian becomes time dependent. Via the Heisenberg equation, we are able to calculate the magnon dynamics

$$\frac{d\langle b_{\bar{k}}^\dagger b_{\bar{k}}\rangle}{dt} = \frac{du_{\bar{k}}}{dt} = 2a(t)\beta_{\bar{k}}w_{\bar{k}} - \gamma_r u_{\bar{k}}, \tag{8a}$$

$$\frac{d\mathrm{Re}\,\langle b_{\bar{k}}^\dagger b_{-\bar{k}}^\dagger\rangle}{dt} = \frac{dv_{\bar{k}}}{dt} = -2[\omega_{\bar{k}} + a(t)\alpha_{\bar{k}}]w_{\bar{k}} - \gamma_r v_{\bar{k}}, \tag{8b}$$

$$\frac{d\mathrm{Im}\,\langle b_{\bar{k}}^\dagger b_{-\bar{k}}^\dagger\rangle}{dt} = \frac{dw_{\bar{k}}}{dt} = 2[\omega_{\bar{k}} + a(t)\alpha_{\bar{k}}]v_{\bar{k}}$$
$$+ 2a(t)\beta_{\bar{k}}(u_{\bar{k}} + 1/2) - \gamma_r w_{\bar{k}}, \tag{8c}$$

where $\alpha_{\bar{k}}$ and $\beta_{\bar{k}}$ depend on which couplings are time dependent. In addition, we include a phenomenological decay rate γ_r in analogy to what has been done for triplone [33]. We solve the coupled differential equations for discretized k_z and discretized DOS of the triangular lattice [34] numerically using a Bulirsch-Stoer algorithm [35] with 1000 time steps per picosecond. In our description, the sublattice magnetization consists of a time-independent part $L_0 = S - \Delta L$ that contains the spin per site reduced by quantum fluctuations $\Delta L = \frac{1}{2N}\sum_{\bar{k}}(\omega_{\bar{k}}/A_{\bar{k}} - 1)$ and a time-dependent part δL: $L = L_0 - \delta L$. The time-dependent change of the sublattice magnetization reads

$$\delta L = \frac{1}{N}\sum_{\bar{k}}\left[\frac{A_{\bar{k}}}{\omega_{\bar{k}}}\langle b_{\bar{k}}^\dagger b_{\bar{k}}\rangle - \frac{B_{\bar{k}}}{\omega_{\bar{k}}}\mathrm{Re}\,\langle b_{\bar{k}}^\dagger b_{-\bar{k}}^\dagger\rangle\right]. \tag{9}$$

Physical meaningful results require that the sublattice magnetization is not greater than S. Therefore, we restrict ourselves to small $|\delta L|$, but δL may be negative representing an increase of L for short time intervals as along as $\Delta L + \delta L \geqslant 0$.

Inserting the experimental values of the parameters, the equations are solved and the time dependence of the change of the longitudinal component of $\bar{L}$ (δL) is plotted in Figs. 7(a) and 7(c). The purely longitudinal dynamics of the order parameter exhibits oscillations with the same frequency of the driving phonons [Fig. 7(c)]. It is worth noting that this constitutes a novel microscopic mechanism to control magnetic systems which has been previously proposed only for spin ensembles lacking a long-range order [33]. In fact, the recently proposed nonlinear phononics applied to magnetic materials is based on the idea that resonantly driven infrared-active phonons couple to Raman-active phonons, which in turn modify the exchange integral [29]. In our case Raman-active phonon modes induce pairs of coherent magnon modes, in a parametric process which fulfills the energy- and wave-vector-conservation laws. Uniquely to our mechanism, the dynamics is purely longitudinal as the total spin is conserved, i.e., $\Delta S = 0$. The coherent magnons dephase because many magnon pairs, not only the pair resonant with the frequency matching the phonon, contribute to δL, although not resonantly and thus with a smaller amplitude. Dephasing is thus fully captured by our theory. Additional possible scattering events are taken into account at a phenomenological level by the γ_r parameter. The dephasing of the coherent oscillations
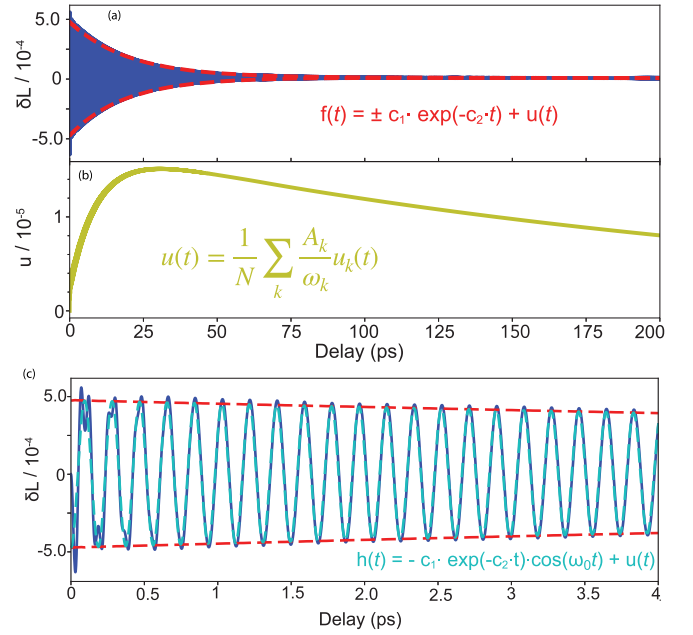

FIG. 7. Spin-lattice coupling. Predicted nonequilibrium dynamics of the L vector on the 200 ps (a) and 4 ps (c) timescale. The increase of the magnon population [$u(t)$] is shown in (b). The function $h(t)$ is a fit to δL. The function $f(t)$ fits the envelope of the spin dynamics, obtained for $c_1 = (4.74 \pm 0.04) \times 10^{-4}$ and $c_2 = (0.0515 \pm 0.0007)\,\mathrm{ps}^{-1}$.

also triggers incoherent longitudinal dynamics of the order parameter. The harmonic component of the signal decays with a rate proportional to the damping of the driving lattice mode [Figs. 7(a)–7(c)]. Interestingly, the population of a specific magnon mode, expressed by $u_{\bar{k}}$, grows [Fig. 7(b)] effectively demagnetizing both sublattices simultaneously. We emphasize that this result is not trivial: typically light-induced spin dynamics is described by means of an additional source term in the Landau-Lifschitz equations of motion, which mimics the action of the optical excitation on spins. Our approach is inherently different. We modify the Hamiltonian of the magnetic system by means of a term describing how the most fundamental magnetic interaction is affected by laser pulses (via the generation of phonons). Then we solve the quantum mechanical Heisenberg equation of motion, obtaining the dynamics of the antiferromagnetic order parameter.

As already discussed in Sec. II, our experimental geometry is sensitive to magneto-optical effects, which are in principle able to reveal the spin dynamics predicted by means of our model. The magneto-optical measurements are discussed in the next section.

VI. SINGLE-COLOR MAGNETO-OPTICAL PUMP-PROBE MEASUREMENTS

The magneto-optical measurements are performed with the setup described in Sec. II and shown in Fig. 6(a). The time-dependent measurements of the rotation of the polarization θ shown in Figs. 8(a)–8(c) are performed in the same experimental conditions employed for collecting the data in Figs. 6(b) and 6(d), so that a direct comparison with the $\Delta T/T$
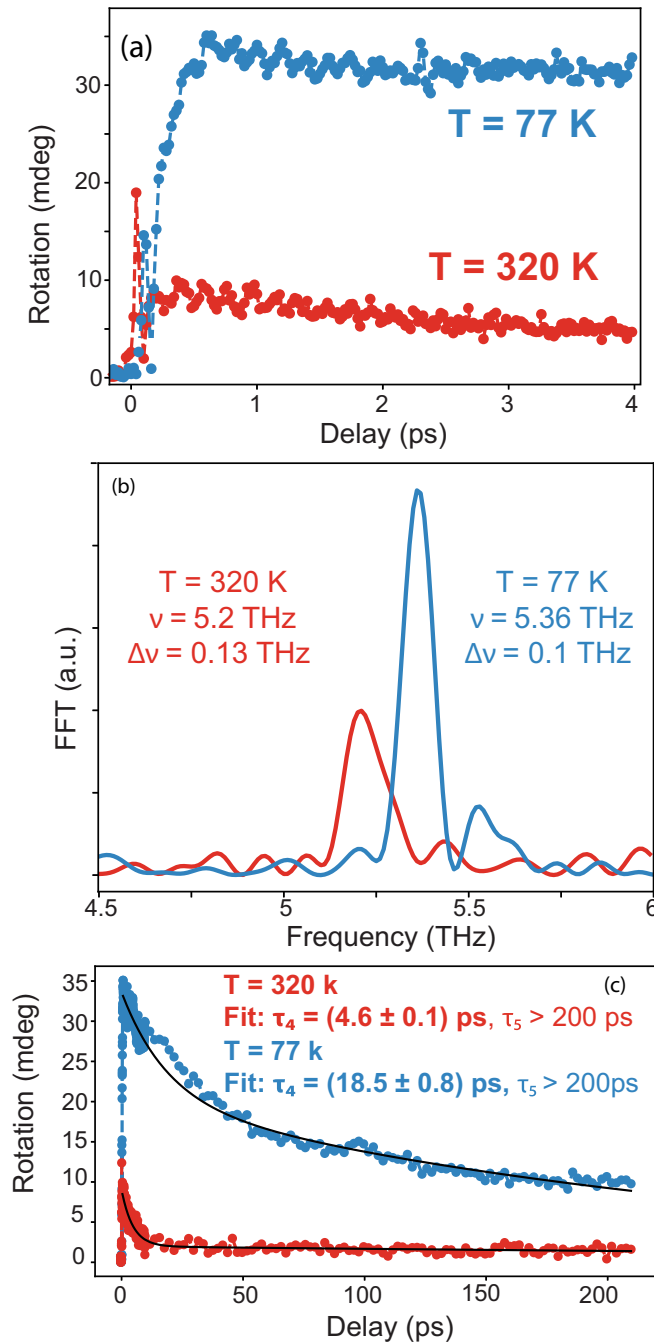
FIG. 8. (a) Rotation of the polarization in the paramagnetic and antiferromagnetic phase in a 4 ps temporal range. (b) Fourier transform of the data in (a). (c) Rotation of the polarization in the paramagnetic and antiferromagnetic phase is shown in a 200 ps temporal region.

dynamics can be carried on. In the first 4 ps subsequent the photoexcitation, θ oscillates at the 5.3 THz phonon frequency both in the paramagnetic and in the antiferromagnetic phase. The Fourier transform of the data reported in Fig. 8(b) confirms the observations discussed in Fig. 6(c) and coupling of phonons to the magnetic system. The dynamics of θ in a 200 ps time window [Fig. 8(c)] departs from $\Delta T/T$. The femtosecond relaxation dynamics τ_1, which is ascribed to

electron-phonon interaction, is not present. A temperature-dependent picosecond τ_4 and a much longer dynamics τ_5, which is not completely exhausted in the 200 ps range analyzed here, are observed.

We compare the $\Delta T/T$ and θ measurements by expressing the interaction between α-MnTe and the probe beam in terms of the dielectric tensor (see Sec. II). The rotation of the polarization cannot express a magneto-optical effect linear in the antiferromagnetic vector, since an antiferromagnetic counterpart of the Faraday effect is symmetry forbidden in a centrosymmetric material [36] such as α-MnTe. The symmetry analysis of α-MnTe reported in Sec. II points at active quadratic magneto-optical effects, common in antiferromagnets [8,17], such as magnetic linear dichroism. This effect is expressed by the rotation of the polarization of the probe, which depends on the order parameter via contributions proportional to $L\Delta L$. This is consistent with the measurements of ultrafast longitudinal and transversal dynamics of the Néel vector via second order magneto-optics [8,17,20,21].

Following this discussion it is thus tempting to ascribe the origin of the oscillations detected in Fig. 8(a) to coherent spin dynamics. Although this effect is predicted by the model and its detection is symmetry allowed in our experimental configuration, we cannot neglect that a nonmagnetic contribution to the rotation in Fig. 8(a) [Imϵ_{ii}^0 in Eq. (2)] is present for sure, since the 5.3 THz phononic oscillations are observed also above the ordering temperature. Moreover, the predicted coherent magnetic oscillations have the same frequency as the phonon mode, as a result of the parametric process. A quantitative decoupling of the lattice and spin contributions to the oscillations requires additional measurements. Differently, the incoherent dynamics can be straightforwardly ascribed to spin dynamics.

The incoherent contributions to the signal is considered by comparing the measurements performed in the paramagnetic and antiferromagnetic phases of α-MnTe. The amplitude of the rotation signal [Fig. 8(a)] is significantly affected, decreasing by a factor of 3 in the paramagnetic phase, while this is not the case for $\Delta T/T$ [Fig. 6(b)]. This is an evidence of the magnetic contributions to the rotation measurements. Moreover, the rotation detected in a 200 ps time window [Fig. 8(c)] deviates from $\Delta T/T$ as well. In particular, τ_4 increases from $\tau_4 = (4.6 \pm 0.1)$ ps to $\tau_4 = (18.5 \pm 0.8)$ ps when the long-range order is established. These values with their error bars are different from the time constants observed in the optical measurements [Fig. 6(d)]. From the linewidth of the lattice mode [Fig. 6(c)], we estimate its lifetime to be ≈ 10 ps, which is on the same order of magnitude of the fitted value of τ_4 in the antiferromagnetic phase. Our model predicts that the lifetime of the 5.3 THz phonon determines the timescale of the sublattice demagnetization, i.e., the envelope of the harmonic signal shown in Figs. 7(a) and 7(c), which can be measured via magnetic linear dichroism [8,17,20,21]. We thus ascribe τ_4 to the sublattice demagnetization. The blue curve in Fig. 8(a) exhibits a contribution at a subpicosecond timescale. We do not interpret this component of the signal as ultrafast demagnetization as, unlike metals, a semiconductor does not possess the free electrons necessary to photoinduce the femtosecond quench of the magnetic order. To the best of our knowledge, a femtosecond demagnetization of a dielectric or semiconductor

is yet to be reported. As a matter of fact, experimental observations in magnetic semiconductors demonstrate that the first picosecond of laser-driven spin dynamics can display even an enhancement of the magnetization [37], instead of the demagnetization ubiquitous in metals [38,39]. Identifying the origin of the subpicosecond contribution to the signal goes beyond the scope of the present paper. From the results of our model, we expect the τ_4 demagnetization to be driven by the photoinduced phonons. Nevertheless, we note that also electronic effects could play a role, as the pump photon energy is tuned above the band gap. This contribution should not be dominant in our experiment, since the timescale of the demagnetization (τ_4) does not match the timescale of the electronic relaxation observed in the transient transmissivity (τ_1). However, we cannot quantitatively disentangle the electronic and lattice contributions to the signal.

We observe that our sample is in a multidomain state. It may thus be expected that the magneto-optical signal should be averaged out. However, this is not the case: recent theoretical and experimental results [40,41] show that a multidomain antiferromagnet can exhibit both coherent and incoherent spin dynamics. In fact, the efficiency of the optical excitation (for both coherent and incoherent processes) differs for different domains, as it is defined by the direction of spins with respect to the polarization of light. The same argument applies to the magneto-optical effects employed to monitor spin dynamics. Consequently, the contribution of some domains is dominant and hence a net signal can be detected.

The idea that optically excited phonons can induce spin dynamics via a modification of the exchange interaction was put forward in the case of a dielectric ferrimagnet [42] and weak ferromagnet [30]. However, our approach and our work are essentially different. In the former case [42], the optically driven phonons decay via scattering with other lattice modes, so that the lattice itself is a laser-heated thermal bath, with temperature higher than the magnetic system. In this context, stochastic fluctuations of the ionic positions affect the exchange interaction, which in turn triggers the demagnetization of the sublattices. In the latter case [30], the resonant pumping of phonons results in the generation of coherent magnons at the center of the Brillouin zone, with a modified frequency in comparison with the dispersion relation. Our model describes the perturbation of the exchange by means of a specific coherent lattice mode. The corresponding microscopic mechanism is totally different, as it entails a phonon-driven parametric generation of counterpropagating magnon pairs, not at the center of the Brillouin zone. Additionally, also the spin dynamics calculated in the present work is unique since the coherent harmonic component of L shown in Fig. 7(c) does not appear in the literature [42]. The oscillating signal detected in Ref. [30] corresponds to a macroscopic spin precession of the magnetization of a weak ferromagnet and not to the solely longitudinal coherent motion of L described in our model. We finally stress again that Ref. [30] relies on static, average shifts of the exchange couplings, while we do not need to take this effect into account.

VII. CONCLUSION

The essence of spintronics consists of the coupling between charges and spins. Here we demonstrate that in a room-temperature antiferromagnetic semiconductor optical phonons couple dynamically to both spin and charges at the ultrafast timescale. It can thus be envisaged that a resonant pumping of the proper phonon mode, which is symmetry allowed in the case of α-MnTe [43], represents a channel to control both spin and charges in semiconductors even in a nonlinear dynamical fashion, a cornerstone for ultrafast semiconductor spintronics. The concept described in our paper could be extended to atomically thin materials, as an efficient displacive phonon pumping has already been reported for these systems [44].

[1] J. K. Furdyna, Diluted magnetic semiconductors, J. Appl. Phys. **64**, R29 (1988).

[2] T. Dietl, A ten-year perspective on dilute magnetic semiconductors and oxides, Nat. Mater. **9**, 965 (2010).

[3] D. D. Awschalom and M. E. Flatté, Challenges for semiconductor spintronics, Nat. Phys. **3**, 153 (2007).

[4] T. Jungwirth, J. Sinova, A. Manchon, X. Martí, J. Wunderlich, and C. Felser, The multiple directions of antiferromagnetic spintronics, Nat. Phys. **14**, 200 (2018).

[5] T. Jungwirth, X. Martí, P. Wadley, and J. Wunderlich, Antiferromagnetic spintronics, Nat. Nanotechnol. **11**, 231 (2016).

[6] V. Baltz, A. Manchon, M. Tsoi, T. Moriyama, T. Ono, and Y. Tserkovnyak, Antiferromagnetic spintronics, Rev. Mod. Phys. **90**, 015005 (2018).

[7] D. Bossini, S. D. Conte, Y. Hashimoto, A. Secchi, R. V. Pisarev, T. Rasing, G. Cerullo, and A. V. Kimel, Macrospin dynamics in antiferromagnets triggered by sub-20 femtosecond injection of nanomagnons, Nat. Commun. **7**, 10645 (2016).

[8] P. Nemec, M. Fiebig, T. Kampfrath, and A. V. Kimel, Antiferromagnetic opto-spintronics, Nat. Phys. **14**, 229 (2018).

[9] H. J. Zeiger, J. Vidal, T. K. Cheng, E. P. Ippen, G. Dresselhaus, and M. S. Dresselhaus, Theory for displacive excitation of coherent phonons, Phys. Rev. B **45**, 768 (1992).

[10] R. Merlin, Generating coherent THz phonons with light pulses, Solid State Commun. **102**, 207 (1997).

[11] W. Szuszkiewicz, E. Dynowska, B. Witkowska, and B. Hennion, Spin-wave measurements on hexagonal MnTe of

NiAs-type structure by inelastic neutron scattering, Phys. Rev. B **73**, 104403 (2006).

[12] V. V. Rzhevskii, Features of the E_{2g} phonon mode in MgB$_2$, Moscow Univ. Phys. Bull. **64**, 98 (2009).

[13] D. Kriegner, K. Výborný, K. Olejník, H. Reichlová, V. Novak, X. Martí, J. Gazquez, V. Saidl, P. Nemec, V. V. Volobuev, G. Springholz, V. Holý, and T. Jungwirth, Multiple-stable anisotropic magnetoresistance memory in antiferromagnetic MnTe, Nat. Commun. **7**, 11623 (2016).

[14] S. Mu, R. P. Hermann, S. Gorsse, H. Zhao, M. E. Manley, R. S. Fishman, and L. Lindsay, Phonons, magnons, and lattice thermal transport in antiferromagnetic semiconductor MnTe, Phys. Rev. Materials **3**, 025403 (2019).

[15] S. R. Mobasser and T. R. Hart, Raman scattering from phonons and magnons In magnetic semiconductor, MnTe, 1985 Los Angeles Techn. Symp. **0524**, 137 (1985).

[16] L. Landau and E. Lifshitz, *Electrodynamics of Continuous Media* (Pergamon, New York, 1981).

[17] D. Bossini and T. Rasing, Femtosecond optomagnetism in dielectric antiferromagnets, Phys. Scr. **92**, 024002 (2017).

[18] J. Ferre and G. A. Gehring, Linear optical birefringence of magnetic crystals, Rep. Prog. Phys. **47**, 513 (1984).

[19] R. Birss, *Symmetry and Magnetism* (Wiley & Sons, New York, 1966).

[20] D. Bossini, A. M. Kalashnikova, R. V. Pisarev, Th. Rasing, and A. V. Kimel, Controlling coherent and incoherent spin dynamics by steering the photoinduced energy flow, Phys. Rev. B **89**, 060405(R) (2014).

[21] V. Saidl, P. Nemec, P. Wadley, V. Hills, R. P. Campion, V. Novak, K. W. Edmonds, F. Maccherozzi, S. S. Dhesi, B. L. Gallagher, F. Trojanek, J. Kunes, J. Zelezny, P. Maly, and T. Jungwirth, Optical determination of the Neel vector in a CuMnAs thin-film antiferromagnet, Nat. Photonics **11**, 91 (2017).

[22] C. Ferrer-Roca, A. Segura, C. Reig, and V. Munoz, Temperature and pressure dependence of the optical absorption in hexagonal MnTe, Phys. Rev. B **61**, 13679 (2000).

[23] D. Bossini, M. Terschanski, F. Mertens, G. Springholz, A. Bonanni, G. S. Uhrig, and M. Cinchetti, Exchange-mediated magnetic blue-shift of the band-gap energy in the antiferromagnetic semiconductor MnTe, New J. Phys. **22**, 083029 (2020).

[24] J. Zhang, Q. Lian, Z. Pan, W. Bai, J. Yang, Y. Zhang, X. Tang, and J. Chu, Spin-phonon coupling and two-magnons scattering behaviors in hexagonal NiAs-type antiferromagnetic MnTe epitaxial films, J. Raman Spectrosc. **51**, 1383 (2020).

[25] M. Hase, M. Katsuragawa, A. M. Constantinescu, and H. Petek, Coherent phonon-induced optical modulation in semiconductors at terahertz frequencies, New J. Phys. **15**, 055018 (2013).

[26] C. Manzoni and G. Cerullo, Design criteria for ultrafast optical parametric amplifiers, J. Opt. **18**, 103501 (2016).

[27] Z. Tong, S. Li, X. Ruan, and H. Bao, Comprehensive first-principles analysis of phonon thermal conductivity and electron-phonon coupling in different metals, Phys. Rev. B **100**, 144306 (2019).

[28] Y. Tomono, Y. Tomono, T. Takaoka, M. Yajima, Y. Tanokura, and N. Jinda, Temperature dependence of lattice vibration frequencies of KNiF$_3$ in connection with antiferromagnetism, J. Phys. Soc. Jpn. **59**, 579 (1990).

[29] M. Fechner, A. Sukhov, L. Chotorlishvili, C. Kenel, J. Berakdar, and N. A. Spaldin, Magnetophononics: Ultrafast

spin control through the lattice, Phys. Rev. Mater. **2**, 064401 (2018).

[30] D. Afanasiev, J. R. Hortensius, B. A. Ivanov, A. Sasani, E. Bousquet, Y. M. Blanter, R. V. Mikhaylovskiy, A. V. Kimel, and A. D. Caviglia, Ultrafast control of magnetic interactions via light-driven phonons, Nat. Mater. **20**, 607 (2021).

[31] K. Deltenre, D. Bossini, F. B. Anders, and G. S. Uhrig, Lattice-driven femtosecond magnon dynamics in α-MnTe, Phys. Rev. B **104**, 184419 (2021).

[32] T. Holstein and H. Primakoff, Field dependence of the intrinsic domain magnetization of a ferromagnet, Phys. Rev. **58**, 1098 (1940).

[33] M. Yarmohammadi, C. Meyer, B. Fauseweh, B. Normand, and G. S. Uhrig, Dynamical properties of a driven dissipative dimerized $S = 12$ chain, Phys. Rev. B **103**, 045132 (2021).

[34] T. Hanisch, B. Kleine, A. Ritzl, and E. Müller-Hartmann, Ferromagnetism in the Hubbard model: Instability of the Nagaoka state on the triangular, honeycomb and kagome lattices, Ann. Phys. **507**, 303 (1995).

[35] W. H. Press, S. A. Teukolsky, W. T. Vetterling, and B. P. Flannery, *Numerical Recipes 3rd Edition: The Art of Scientific Computing*, 3rd ed. (Cambridge University Press, Cambridge, 2007).

[36] B. B. Krichevtsov, V. V. Pavlov, V. N. Gridnev, and R. V. Pisarev, Spontaneous non-reciprocal reflection of light from antiferromagnetic Cr$_2$O$_3$, J. Phys.: Condens. Matter **5**, 8233 (1993).

[37] F. Liu, T. Makino, T. Yamasaki, K. Ueno, A. Tsukazaki, T. Fukumura, Y. Kong, and M. Kawasaki, Ultrafast Time-Resolved Faraday Rotation In EuO Thin Films, Phys. Rev. Lett. **108**, 257401 (2012).

[38] B. Koopmans, G. Malinowski, F. D. Longa, D. Steiauf, M. Faehnle, T. Roth, M. Cinchetti, and M. Aeschlimann, Explaining the paradoxical diversity of ultrafast laser-induced demagnetization, Nat. Mater. **9**, 259 (2010).

[39] A. Kirilyuk, A. V. Kimel, and T. Rasing, Ultrafast optical manipulation of magnetic order, Rev. Mod. Phys. **82**, 2731 (2010).

[40] D. Bossini, M. Pancaldi, L. Soumah, M. Basini, F. Mertens, M. Cinchetti, T. Satoh, O. Gomonay, and S. Bonetti, Ultrafast Amplification and Nonlinear Magnetoelastic Coupling of Coherent Magnon Modes in an Antiferromagnet, Phys. Rev. Lett. **127**, 077202 (2021).

[41] O. Gomonay and D. Bossini, Linear and nonlinear spin dynamics in multi-domain magnetoelastic antiferromagnets, J. Phys. D **54**, 374004 (2021).

[42] S. F. Maehrlein, I. Radu, P. Maldonado, A. Paarmann, M. Gensch, A. M. Kalashnikova, R. V. Pisarev, M. Wolf, P. M. Oppeneer, J. Barker, and T. Kampfrath, Dissecting spin-phonon equilibration in ferrimagnetic insulators by ultrafast lattice excitation, Sci. Adv. **4**, eaar5164 (2018).

[43] S. J. Cyvin, J. E. Rauch, and J. C. Decius, Theory of hyper-Raman effects (nonlinear inelastic light scattering): Selection rules and depolarization ratios for the second-order polarizability, J. Chem. Phys. **43**, 4083 (1965).

[44] C. Trovatello, H. P. C. Miranda, A. Molina-Sanchez, R. Borrego-Varillas, C. Manzoni, L. Moretti, L. Ganzer, M. Maiuri, J. Wang, D. Dumcenco, A. Kis, L. Wirtz, A. Marini, G. Soavi, A. C. Ferrari, G. Cerullo, D. Sangalli, and S. D. Conte, Strongly coupled coherent phonons in single-layer MoS$_2$, ACS Nano **14**, 5700 (2020).